Structure and radiation response of anion excess bixbyite Gd$_2$Ce$_2$O$_7$

Maulik Patel [*]

The University of Liverpool, School of Engineering, Department of Mechanical, Materials and Aerospace Engineering,
Liverpool L69 3GH, United Kingdom

Jeffery Aguiar [†]

Department of Materials Science and Engineering, The University of Utah, 301 President's Circle, Salt Lake City, Utah 84109, USA

Kurt Sickafus [‡]

Los Alamos National Laboratory, Materials Science and Technology Division, Los Alamos, New Mexico 87545, USA
and The University of Tennessee, Department of Materials Science and Engineering, Knoxville, Tennessee 37996, USA

Gianguido Baldinozzi [§]

Université Paris-Saclay, CentraleSupélec, Centre national de la recherche scientifique (CNRS), Structures, Propriétés et Modélisation des
Solides, 91190 Gif-sur-Yvette, France

The crystal structure analysis of Gd$_2$Ce$_2$O$_7$ reveals that it crystallizes in a bixbyite-type symmetry ($I2_1 3$). Analysis of the structure suggests a randomly occupied cation sublattice with infinite correlation length associated with long-range ordered anion sublattice with half of the vacant sites of an ideal bixbyite filled, hence the name anion-excess bixbyite. Ion irradiation experiments and quantitative x-ray diffraction analysis were used to study the separate response of the anion sublattice to swift heavy ion radiation. Analysis of anion and cation correlation lengths as a function of fluence shows that the topological disorder on the anion sublattice grows faster than that on the cation sublattice. The microstructural response at increasing radiation fluences leads to a decrease of the strain after an initial increase, while the variance of the strain increases following the increase of the microdomain wall density. This particular behavior seems responsible for the exceptional radiation resistance of this system that does not display any significant amorphization, even at the highest fluence.

I. INTRODUCTION

The family of oxygen deficient fluorite compounds has gained significant interest as systems for minor actinides disposal and for understanding spent fuel chemistry, though they can be interesting systems also for their magnetic properties, their low thermal conductivity, and as ionic conductors [1–6]. Apart from these technological interests, these oxides provide a fascinating playground to explore the order mechanisms arising from flexible aliovalent doping and nonstoichiometry [7–15]. In most of these compounds, the preferred mechanism of charge compensation of the aliovalent doping is the creation of O vacancies. In some of these compounds, cation and anion vacancies do order long range (e.g., pyrochlores and weberites), while in other ones, only the oxygen vacancies order (as, for instance, the β, γ, and δ phases [16–18] in the mixed oxides of scandium with zirconium or hafnium). In other compounds, neither cations nor anions exhibit long-range site selectivity (as, for instance, Y$_2$Zr$_2$O$_7$). These characteristics are particularly interesting because they may facilitate the

separation of the specific response of the cation and anion sublattices to radiation damage. While structural changes induced by irradiation have been extensively studied in the systems where cations are initially ordered [19–23] and in systems where both sublattices do not display long-range order, the irradiation behavior of fluorite-related oxide systems where the cations are randomly distributed but the anions are highly ordered has not been quantitatively explored yet. This is partly due to the relative rarity of such model systems. The search for such a system has led us to take a closer look at the phases formed in the CeO$_2$-Gd$_2$O$_3$ pseudobinary system. In this system, while a single phase of fluorite structure oxide is observed in the Ce-rich region, a C-type phase is encountered in the Gd-rich region. This is also generally true for other CeO$_2$-Ln_2O$_3$ systems (where Ln is a lanthanide element) [9]. Among this class of compounds, with compositions close to a morphotropic boundary, Gd$_2$Ce$_2$O$_7$ was previously reported to crystallize with a structure related to a bixbyite phase [24,25]. In this compound, the statistically weighted mean cation radius $\langle r_M \rangle$ is large enough to favor the eightfold coordination of the cation typical of a fluorite phase against the possible structural polymorphism driven by the preference for an octahedral environment typical of a smaller-sized cation. However, this is not the only specific feature of this compound.

———————
[*]maulik@liverpool.ac.uk
[†]Jeffery.Aguiar@gmail.com
[‡]kurt@lanl.gov
[§]gianguido.baldinozzi@centralesupelec.fr

When a mixture of cations shares a single crystallographic site, the determination of short-range properties related to the exact cation distribution is a complex task that requires a precise analysis of the diffuse scattering. Nevertheless, long-wavelength collective properties (elastic properties) that can promote the vacancy ordering might not be extremely sensitive to these short-range details. When the compositional fluctuations are small to a scale much larger than the lattice spacing, it can be possible to coarse-grain the material composition and describe the site occupancy using a scalar composition field that is the average of the elemental site occupancies over several cells. The price we pay with this formalism is that we lose the contribution of the short-range fluctuations to the entropy. In this respect, $Gd_2Ce_2O_7$ is particularly interesting because not only the weighted mean cation radius has an optimum value for the fluorite structure, but also the size mismatch between the two cation vanishes. This size mismatch is better defined by the statistical variance of the distribution of the radii ($\sigma^2 = \langle r_M^2 \rangle - \langle r_M \rangle^2$, that is the second central moment of the radii distribution [26]). Indeed, a mismatch can effectively promote cation order and also favor cation offsite displacements from their ideal fluorite positions. Also, it can help in stabilizing long-range cooperative displacements that can actively interfere with the ordering of the O vacancies. This effect is minimal or even absent in $Gd_2Ce_2O_7$; therefore, in this system, the cations have a neutral or minimal influence on the long-range order in the anion sublattice, leading to a decoupled behavior for the characteristic patterns of the O vacancies.

This characteristic property of $Gd_2Ce_2O_7$ is particularly interesting because it allows us to study the specific response of the anion sublattice to radiation damage. In this paper, (1) we present a careful analysis of the characteristic of the O vacancy order in the pristine structure of $Gd_2Ce_2O_7$, whose hallmark is the long-range order of the anions decoupled from any significant site selectivity of the cations; and (2) we follow the radiation response of the anion sublattice where the significant mobility of the O vacancies just above room temperature provides an efficient mechanism for healing the radiation damage occurring in this system. Indeed, this fluorite-related system does not display any significant amorphization even at the highest fluences of the swift heavy ion irradiation experiment.

II. EXPERIMENTAL PROCEDURES

Powders of cerium dioxide (CeO_2, 99.99%) and gadolinium sesquioxide (Gd_2O_3, 99.99%) purchased from Alfa Aesar were calcined at 700 °C and weighed to obtain a 2:2:7 stoichiometric ratio of Gd : Ce : O. These mixtures were ground in isopropanol medium in a large agate mortar for 12 h. The powder mixture was cold pressed into disks of 8 mm diameter and 1 mm thickness using a tungsten carbide die and plunger. The disks were then sintered twice in air, first at 1200 °C for 24 h and then at 1400 °C for 48 h with the heating and cooling rates of 2 °C/min and with intermittent regrinding between the two sintering cycles.

To study the radiation response of $Gd_2Ce_2O_7$, discs of 8 mm diameter and 2 mm thickness were irradiated at room temperature by 92 MeV Xe^{26+} ions at IRRSUD facility at

GANIL, France, using fluences ranging from 10^{11} to 10^{14} ions cm^{-2}. The flux of ions during irradiation was 10^9 ions $cm^{-2} s^{-1}$, and the sample surface was kept normal to the ion beam direction. X-ray diffraction (XRD) measurements were performed only on samples irradiated with fluences $>10^{12}$ ions cm^{-2}, which corresponds to the conditions of a uniformly irradiated surface due to multiple track overlaps. The range and stopping powers of 92 MeV Xe^{26+} ions in $Gd_2Ce_2O_7$ were estimated using Monte Carlo simulation program SRIM [27]. The plot of nuclear and electronic energy loss vs depth shows that these ions lose energy primarily in the electronic stopping regime [Fig. 1(a)].

The projected range of these ions in $Gd_2Ce_2O_7$ is 9 μm, while the penetration depth of Cu $K\alpha$ x rays used for the XRD experiments is always <2.5 μm, even at high angles θ formed by the impinging x-ray beam and the sample surface [Fig. 1(b)]. Hence, XRD can be carried out in a bisecting reflection geometry to assess the structural modifications in the pristine and damaged layers of the irradiated samples. The implanted and pristine layers in the irradiated pellets do not contribute to the intensity of the scattered beam.

X-ray powder diffraction experiments were performed to characterize the structure of the as-synthesized samples and the pellets used for the irradiation experiment. XRD was performed using a Bruker D8 Advance diffractometer equipped with a Göbel mirror for Cu $K\alpha$ radiation and a NaI scintillation detector. For reasons mentioned above, data collection was performed in a θ-θ geometry, performing symmetric step scans of the detector and x-ray source ($\Delta 2\theta = 0.02°$, and 2θ range 10–80°) and a step time of 2 s per step. Rietveld refinements were performed using the software XND [28]. The parameters defining the instrumental broadening (transfer function) of the diffractometer were determined using a LaB_6 NIST-660C standard sample stored in argon.

Electron transparent transmission electron microscopy (TEM) samples were prepared by pulverizing and crushing powder samples. Powder was equally dispersed on a holey carbon grid using high-purity ethyl alcohol and subsequently observed inside a TEM. A high-tilt FEI Tecnai was operated in TEM and diffraction modes at 200 kV. For high-resolution microscopy, the sample was oriented preferentially utilizing selected-area electron diffraction (SAED) and calibrated charge-coupled device (CCD) camera. Excitation errors were mitigated by comparing intensity symmetry relating the principal beam spot in the accompanying two-dimensional diffraction pattern. The spot electron intensity in electrons per pixel was quantitatively compared inside Digital Micrograph. The CCD camera was again normalized and stabilized over hours of continuous operation prior to observing the sample to mitigate spurious background drift and differences in counting rate statistics.

III. PRISTINE $Gd_2Ce_2O_7$

A. Symmetry analysis of the pristine phase

The determination of the structure of $Gd_2Ce_2O_7$ cannot be performed using usual crystallographic methods because of the difficulty of growing single crystals of suitable size and perfection, a task that is made unmanageable by their
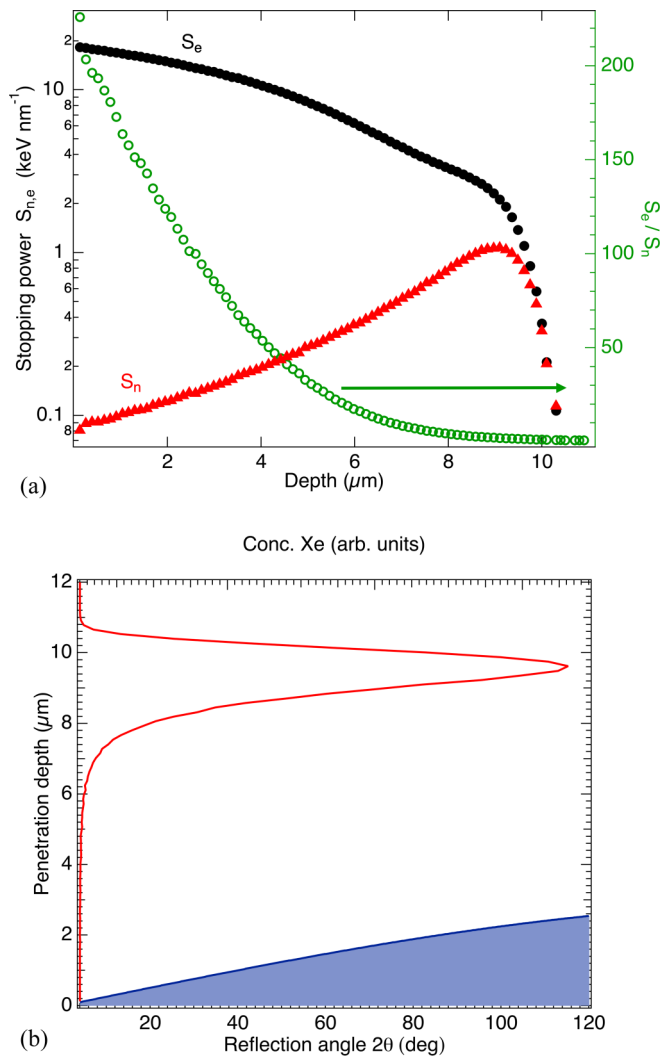
FIG. 1. (a) Electronic vs nuclear energy loss for 92 MeV Xe ions in $Gd_2Ce_2O_7$ as a function of target depth. The ordinate on the left shows electronic (black circles) or nuclear (red triangles) energy losses on a logarithmic scale. The scale on the right shows the ratio of electronic-to-nuclear energy loss (green open circles). (b) Penetration depth of Cu-Kα x rays in $Gd_2Ce_2O_7$ (shaded blue) for the Bragg-Brentano reflection geometry as a function of the scattering angle (2θ, bottom scale). 97% of the scattered intensity comes from the corresponding depth in the sample. Xe implantation profile (red line, top scale). The comparison shows all of the x-ray scattered signal comes from the irradiated region where no significant implantation occurs.

complex twinning systems. Therefore, the crystallographic analysis relies on powder diffraction methods and upon TEM that is effective for examining thin single-crystal regions that are typically untwinned and therefore highly suitable for the analysis of systematic extinctions and symmetry element determination.

The x-ray powder diffraction pattern of pristine $Gd_2Ce_2O_7$ (Fig. 2) can be successfully indexed using a crystal structure akin to the bixbyite C-type Gd_2O_3, though the O stoichiometry of the current compound requires filling half of the vacancies of the bixbyite structure. If the vacancy sublattice is
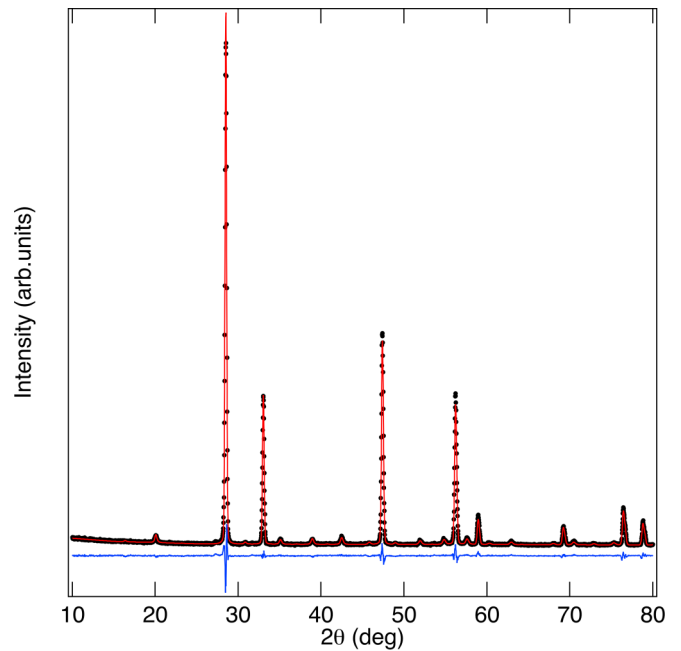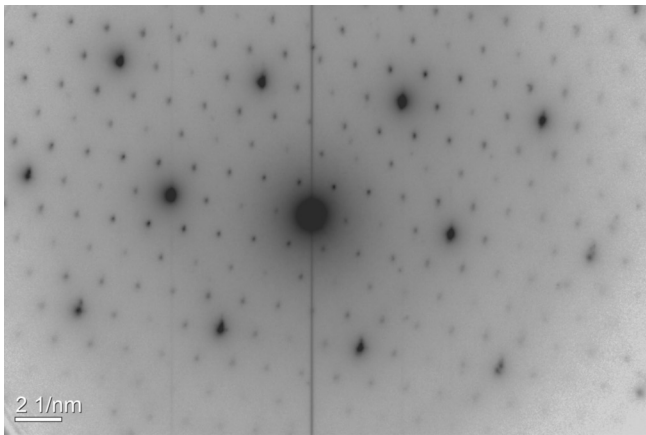

FIG. 2. Observed (black dots), calculated (red solid line) x-ray diffraction (XRD) pattern for pristine $Gd_2Ce_2O_7$ showing the Rietveld fit with a disordered anion excess bixbyite model ($I2_13$, $a = 10.8515(1)$ Å, $Z = 32$). The blue solid line indicates the difference between the observed and calculated patterns.

half-filled at random, then the space group of the long-range structure of this compound is $I a\bar{3}$ as for the ideal bixbyite [30,31]. On the other hand, if the vacancy distribution is not random in the vacancy sublattice, then the symmetry of the system will be described by a subgroup of this disordered parent structure. To assess this point, we have used TEM to closely inspect the extinction rules of SAED patterns obtained for selected zone axes.
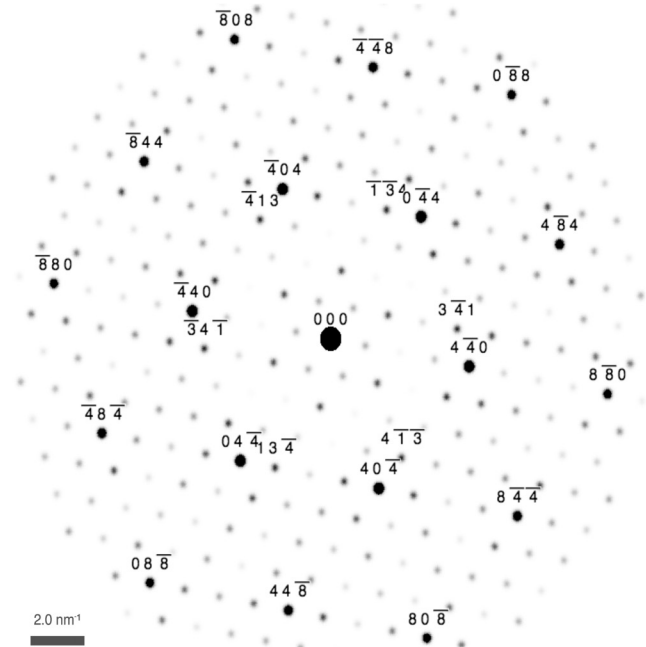
Figure 3(a) displays the [111] zone axis of the reciprocal lattice of a bixbyite structure (the lattice parameter of this cubic structure is twice the one of the corresponding fluorite). In this picture, the reflections of type $\{1\bar{1}0\}$ forming the hexagonal asterism centered at the reciprocal lattice center are clearly observed, though they are in principle forbidden by the a glide of the bixbyite space group. Therefore, a subgroup of $I a\bar{3}$ without glide mirror must be considered. The most symmetric subgroup compatible with this requirement is $I2_13$. The

TABLE I. Initial structural model for the anion excess bixbyite model in the $I2_13$ space group with $a \approx 10.85$ Å, $Z = 32$. The values of β, γ, and δ are $\sim 10^{-2}$.

Atom	Site	x/a	y/a	z/a	Occupancy
M_1	12b	$-\beta$	0	$\frac{1}{4}$	1
M_2	12b	β	0	$\frac{3}{4}$	1
M_3	8a	$\frac{1}{4}$	$\frac{1}{4}$	$\frac{1}{4}$	1
$O_\square$	8a	$\frac{7}{8}$	$\frac{7}{8}$	$\frac{7}{8}$	0
O_1	8a	$\frac{1}{8}+\gamma$	$\frac{1}{8}+\gamma$	$\frac{1}{8}+\gamma$	1
O_2	24c	$\frac{3}{8}+\delta_1$	$\frac{1}{8}+\delta_2$	$\frac{3}{8}+\delta_3$	1
O_3	24c	$\frac{5}{8}-\delta_1$	$\frac{7}{8}-\delta_2$	$\frac{5}{8}-\delta_3$	1

(a)

(b)

FIG. 3. (a) Electron diffraction pattern corresponding to the [111] zone axis in pristine $Gd_2Ce_2O_7$. (b) Simulated electron diffraction pattern using the initial structural model of Table I corresponding to the same [111] zone axis. Full-size versions of (a) and (b) are provided as Supplemental Material [29].

lost symmetry operation can be used to generate the required coset of independent atoms for this structural model. The trial structural model is summarized in Table I. In this model, there are three independent cation sites and four independent anion sites.

The ideal bixbyite vacant sites are represented by the atomic sites $O_\square$ and O_1 in this space group. Choosing different occupancies for these two sites breaks the glide mirror. Therefore, the simplest model that puts intensities on the $\{1\bar{1}0\}$ diffraction spots can be obtained by localizing all the extra O atoms of this compound at either of the two sites. The simulated electron diffraction pattern was generated using SingleCrystal[TM] [32] assuming the O vacancies localized

at $O_\square$ position produce the desired effect represented in Fig. 3(b).

B. Modeling of the x-ray scattered intensities

During an x-ray scattering experiment, the plane-wave impinging beam scatters off the sample, with the emitted radiation proportional to the Fourier transform of the charge density in the sample. The intensity of the scattered beam is then given by the Fourier transform of the equal-time electron density-density correlation function. Diffuse scattering is due to deviations in space and/or time from an average structure that has strict long-range order characteristics. Periodic compositional modulations, twins, domains, or more generally, coherent internal interfaces, that are characteristic of lamellar or shear-type structures [33–37] can mutually interact, leading to complex short-range arrangements that can alter the diffracted intensities.

If an average structure of a disordered crystal can be defined, the scattering intensity can be divided into two additive contributions. The first one comes from the strictly long-range average structure, which is periodic in space, and that produces the usual Bragg scattering. The second one describes the fluctuations in space (and time) around the strict long-range order average structure: this contribution is characterized by shorter range correlations, and it is responsible for the observed diffuse scattering. Neder *et al.* [33] have developed a general method for describing quantitatively the diffuse scattering by correlated microdomains.

In pristine $Gd_2Ce_2O_7$, distinct broadening rules affect the reflections characteristic of the bixbyite superstructure of a given microdomain, where the vacancies order according to a pattern, and the reflections characteristic of the fluorite average structure. Therefore, they require the specific modeling of the diffuse scattering produced by the characteristic order of the O vacancies in their respective correlated microdomains [38]. The information about the short-range order is drawn from the average structure before analyzing diffuse scattering contributions because the intensities of fluorite Bragg peaks at lattice vectors **G** are still predominant. Since fractional occupancies for the anion sublattice are expected, the occupancy modulation and the displacive disorder close to these sites are possibly involved in the production of diffuse scattering at the reciprocal lattice positions **G** + **q** of the bixbyite structure, where **q** is the reciprocal space vector defining the position of the diffuse scattering signal outside of the fluorite reflections located at **G**. The starting model for the refinement uses the structure of Table I. The deviation from the perfect crystalline order springs either from atomic displacement or from atomic substitutions or from a combination of these two effects. The disorder detected in x-ray diffuse scattering experiments can be either dynamic (related to lattice vibrations) or static (displacive, arising from substitutions and crystalline imperfections). In conventional laboratory measurements (and in these experiments in particular), the diffracted beam is measured without energy resolution, and it cannot discriminate between the two aforementioned possibilities. The scattered intensity then gives direct access to instantaneous spatial correlations [39,40] of the order parameter η: $S(\mathbf{q}, t = 0) = |\eta_q|^2$. Here, η_q is the qth component of the Fourier transform of

TABLE II. Structural parameters of the refined anion excess bixbyite model ($I2_13$, a = 10.8515(1) Å, Z = 32). The refinement converges to $R_{wp} = 2.0\%$ and $R_B = 5.96\%$. The refined microdomain size is 34(2) nm. A common isotropic thermal displacement parameter (B) was employed for all atoms.

Atom	Site	x/a	y/a	z/a	Occupancy	B (Å^2)
M_1	12b	$-0.0124(13)$	0	$\frac{1}{4}$	1	0.36(12)
M_2	12b	0.0095(14)	0	$\frac{3}{4}$	1	0.36(12)
M_3	8a	$\frac{1}{4}$	$\frac{1}{4}$	$\frac{1}{4}$	1	0.36(12)
$O_\square$	8a	$\frac{7}{8}$	$\frac{7}{8}$	$\frac{7}{8}$	0	
O_1	8a	0.099(4)	0.099(4)	0.099(4)	1	0.36(12)
O_2	24c	0.395(4)	0.149(5)	0.392(4)	1	0.36(12)
O_3	24c	0.616(4)	0.872(4)	0.632(5)	1	0.36(12)

the spatially dependent modulation wave describing the O vacancy occupancy and the related atomic displacements. The refined structural parameters of this model are summarized in Table II.

C. Structural characteristics of the pristine phase

Table III summarizes the structural motif of $Gd_2Ce_2O_7$, which consists of three different polyhedra. The one centered around M_1 is a distorted cube, the one of M_2 a distorted octahedron, and the one of M_3 a sevenfold coordinated capped octahedron. These polyhedra are stacked into slabs normal to the threefold axis, and they repeat indefinitely. In each slab, there are four vacancies: one of them is in a cage surrounded by three corner-sharing octahedra, the three other ones are in cages formed by two octahedra and a capped octahedron also sharing corners (see Fig. 4). The remainder of the slab contains distorted cubes that share edges with themselves and the two other polyhedra.

This represents a significant difference in the structural motif when compared with pyrochlore structures where only distorted cubes and octahedra are encountered [41]. On the other hand, this variety of polyhedra is characteristic of weberite-type Ln_3MO_7 structures, though they do not share the same connectivities.

The spatial correlation length of the qth component of the order parameter can be obtained from the breadth of the diffuse scattering within the Ornstein-Zernike formalism [42,43]. For this purpose, a Scherrer-type peak broadening
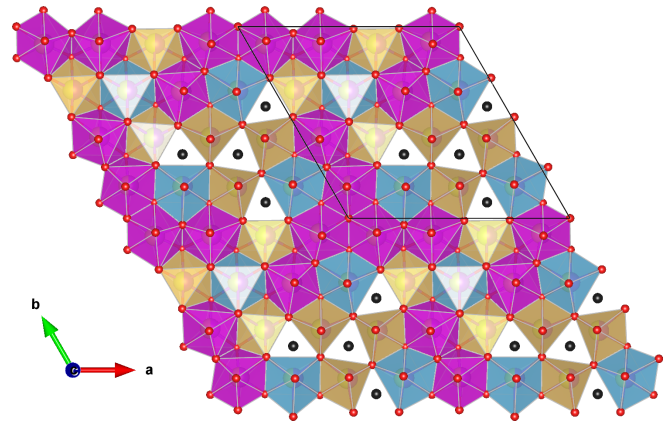

FIG. 4. Polyhedral model of a slab of pristine $Gd_2Ce_2O_7$ obtained by the Rietveld refinement (Table III). Four reference cells are displayed. Gold is the octahedron, purple is the distorted cube, and blue is the capped octahedron. Black spheres materialize the O vacancies.

was included in the correlated Rietveld model [44], providing the characteristic long-range correlation length of the microdomains in real space. Eventually, a microstrain-type peak broadening [45,46] can also be introduced to account for defect-induced elastic fluctuations of the lattice parameter. The measured size of the microdomains of oxygen-excess bixbyite is 34(2) nm. On the other hand, the correlation length of the average structure is 116(2) nm.

IV. RADIATION EFFECTS IN $Gd_2Ce_2O_7$

Figure 5 shows the changes occurring in the x-ray powder diffraction patterns of the pristine and damaged layers of the samples irradiated at several fluences. A staggered plot is also shown in the Supplemental Material [29]. Rietveld refinements of the correlated microdomains in the irradiated samples were performed proceeding with the same model described for the pristine samples. The characteristic broadening of the two families of reflections still provides the measure of the separate correlation lengths describing the anion sublattice (microdomain size) and the cation sublattice (length scale describing the periodic arrangement of the average cation). The refinements also provide a measure of the lattice strain and of its variance (microstrain) as a function of the irradiation

TABLE III. Bond lengths (Å) in the three polyhedra of the refined anion excess bixbyite model.

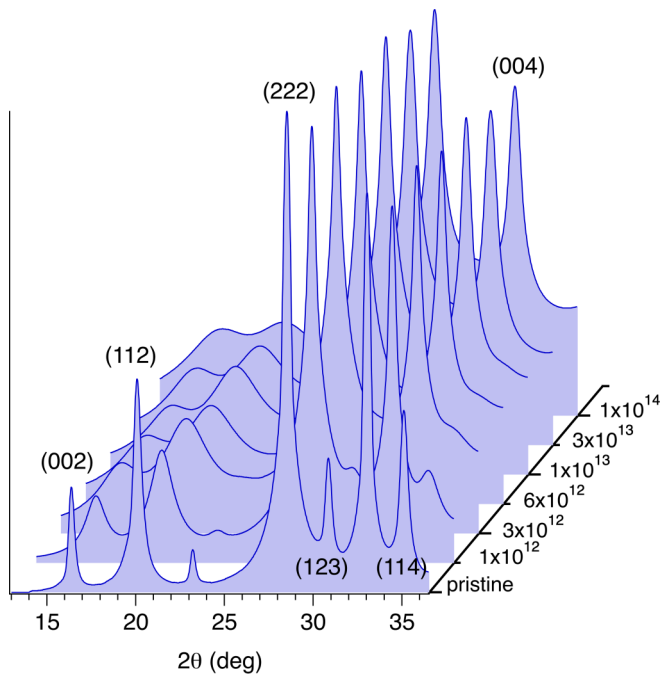| Cube		Octahedron		Capped octahedron	
M_1-O_3	2.20(5)	M_2-O_2	2.03(5)	M_3-$O_\square$	2.35
M_1-O_3	2.20(5)	M_2-O_2	2.03(5)	M_3-O_3	2.35(5)
M_1-O_1	2.30(5)	M_2-$O_\square$	2.41(1)	M_3-O_3	2.35(5)
M_1-O_1	2.30(5)	M_2-$O_\square$	2.41(1)	M_3-O_3	2.35(5)
M_1-O_3	2.41(5)	M_2-O_3	2.41(5)	M_3-O_2	2.46(5)
M_1-O_3	2.41(5)	M_2-O_3	2.41(5)	M_3-O_2	2.46(5)
M_1-O_2	2.46(5)	M_2-O_2	2.46(5)	M_3-O_2	2.46(5)
M_1-O_2	2.46(5)	M_2-O_2	2.46(5)	M_3-O_1	2.84(5)
$\langle M_1$-O$\rangle$	2.34	$\langle M_2$-O$\rangle$	2.30	$\langle M_3$-O$\rangle$	2.47
Volume (Å^3)	21.30		13.81		20.59

FIG. 5. Detail of the x-ray diffraction (XRD) patterns obtained from pristine and irradiated $Gd_2Ce_2O_7$ as a function of increasing fluence. The intensities are represented using a logarithmic scale to display the noticeable broadening of the peaks carrying the information about the periodic stacking of O vacancies in the anion excess bixbyite structure. These sensitive reflections are those that do not fold onto the reflections of an face-centered cubic lattice with halved parameters.

fluence. Upon irradiation, the peaks characteristic of the oxygen excess bixbyite reflections display an accelerated broadening, and the diffuse signal almost fades out at the highest fluence (Fig. 5). On the other hand, the broadening of the reflections characteristic of the average cation periodicity is milder: the crystal periodicity of the cation sublattice is only marginally affected, and there is no clear evidence of any forthcoming amorphization.

Figures 6(a) and 6(b) display the quantitative changes in the characteristic correlation lengths of the two sublattices of $Gd_2Ce_2O_7$. These two correlation lengths contain information about how much the ordered arrangements in each one of the two sublattices influence their distant neighbors.

The disorder quenching effect on the anion sublattice is extremely pronounced: the characteristic correlation length describing the vacancy distribution promptly drops from 34 to ~5 nm [Fig. 6(a)] immediately after the lowest irradiation fluence. Increasing the fluence, this correlation length slowly relaxes to an asymptotic value of ~2 nm. The effect of radiation damage seems to bring the anion sublattice system very far from the equilibrium conditions straight away as soon as the ion irradiation of the sample starts.

The effect on the cation sublattice is also very pronounced in the quenched systems immediately after the lowest irradiation fluence, but it seems to saturate very quickly to a larger asymptotic value, closer to 30 nm [Fig. 6(b)]. This suggests that the absence of any appreciable site selectivity for the
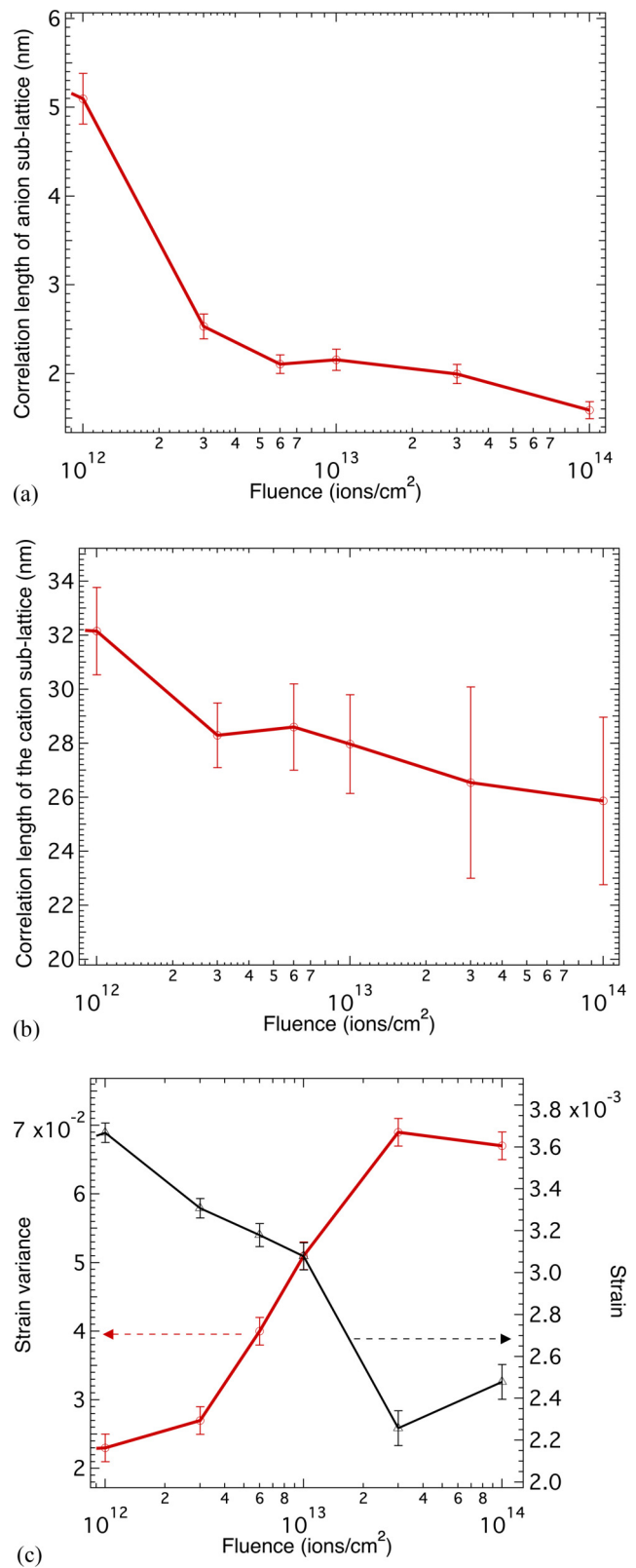

FIG. 6. (a) Correlation length of the anion sublattice as a function of fluence in $Gd_2Ce_2O_7$. This correlation length in pristine samples is ~34 nm. (b) Correlation length of cation sublattice as a function of fluence in $Gd_2Ce_2O_7$. This correlation length in pristine is ~116 nm. (c) Strain and strain variance obtained from Rietveld analysis as a function of the Xe ion fluence. The strain and its variance are near zero for the pristine sample.

cations prevents the glassy behavior observed for the anion sublattice.

To quantify and understand the mechanistic consequences of the radiation-induced defects, changes in the strain and microstrain as a function of fluence are shown in Fig. 6(c). It can be seen that, after a relatively modest increase of the lattice strain after irradiation at the lowest fluence, the strain is reduced at higher fluences, while the strain variance increases. This result is in relatively good agreement with an increased density of topological defects as the irradiation progresses. This is mainly related to the fact that the high density of microdomain walls acts as a sink for accommodating the point defects created during radiation, thus reducing the measured macroscopic strain but increasing its variance.

V. DISCUSSION

Without cation selectivity, the mixed oxides of the rare earths can be related to the binary compound series M_nO_{2n-2}, where n is an integer $\geqslant 4$, famously known as Eyring's homologous series. In these series, typically observed for the Ce, Pr, and Tb oxide systems, the crystal structures corresponding to $n = 4, 7, 9, 10, 11$, and 12 are well established. These phases are fluorite related, and their symmetries are dictated by the particular way the O vacancies order [12]. The problem is generally more complex in ternary compounds when the cations also order and generally compete with the O vacancy distribution, but in the current case, the ionic radius difference and the vanishing cation mismatch (variance) do not favor any significant cation order. The symmetry of these systems is then mainly ruled by the distribution of O vacancies. This characteristic feature seems to be the hallmark of $Gd_2Ce_2O_7$. Nevertheless, the particular oxygen stoichiometry of the current system is not among the the crystal structures found for the binary systems (Eyring's series), but it is at an intermediate position between the trigonal ζ-Pr_9O_{16} ($n = 9$) and the trigonal ι-Pr_7O_{12}-type structure ($n = 7$). These two phases only differ by the spacing of their respective planar defect features, an effect that typically leads to the intergrowth of layers of variable thickness with topotaxial relationships between these two phases in a way like stacking faults.

The oxygen excess bixbyite $Gd_2Ce_2O_7$ requires filling up half of the vacant sites in the C-type bixbyite structure. This unexpected result suggests the vacancy stacking according to a bixbyitelike rule is preferred to the slightly different vacancy stacking of the trigonal ζ and ι phases that have stoichiometries framing the one of the current compound. The apparent attraction for the bixbyite stacking was already discussed in the study of the irradiation behavior of the system δ-$Sc_4Hf_3O_{12}$, where cations do not display any marked long-range order [44].

The fact that pristine $Gd_2Ce_2O_7$ is a wide-gap semiconductor means that boundaries among these correlated microdomains and their dynamics cannot be treated as perfect insulators [34]. The fact that domain walls can be charged or uncharged, straight or curved, makes the assumption of equilibrium structures simply not likely. Depletion and accumulation of O vacancies can occur at or near interfaces and domain walls. Charges can accumulate or leak off with various relaxation times, and these and other causes can

produce long-lived out-of-equilibrium structures because the relaxation mechanism can be kinetically inhibited, eventually leading to states that can have some characteristics of a domain glass.

The reduction of correlation length induced by the ion irradiation can be understood by an analogy with a temperature transformation. During irradiation, the crystalline system undergoes a phase transition from a large collection of ordered microdomains all characterized by an oxygen excess bixbyite structure to a disordered fluorite structure where cation and anion sites are statistically occupied according to their particular stoichiometries. Once the perturbation produced by irradiation is switched off, the single homogeneous disordered phase is suddenly quenched to a broken-symmetry phase where domains of the equilibrium bixbyite phase form and coarsen with time as the system achieves local equilibrium on larger and larger scales. The result of the irradiation experiment suggests that this process of return to equilibrium has two very different length scales for each one of the two sublattices of the crystal.

Since the two cations do not display any prominent tendency to order, their statistical mixing produced by the irradiation lets them almost freely rearrange over relatively large length scales. The moot concept of the theoretical Kauzmann temperature [47], if it exists for these systems, could be useful to describe this transformation with the analogy with a supercooled liquid pattern of O vacancies and their corresponding crystalline state. In the present context, the Kauzmann temperature can loosely describe the temperature at which O vacancy patterns freeze in. This frustrated vacancy arrangement is then responsible for the shorter length-scale characterizing the anion sublattice and for the appearance of the topological defects separating the regions characterized by a different orientational order of the oxygen excess bixbyite phase.

The increase of the strain variance can be loosely interpreted as the transition from a system characterized by an auxiliary field which varies smoothly in space to a system with a defined order parameter in each of the oxygen excess bixbyite microdomains (this order parameter has a constant value everywhere except in correspondence with the microdomain walls). This describes a situation where the frustrated local order is not strong enough to impose its orientational symmetry long range, and therefore, it exists in a long-range structure that is all the same characterized by cations that live in a periodic space.

The study of pristine and irradiated $Gd_2Ce_2O_7$ provides a complex picture of a system that retains a considerable periodic order even at high irradiation fluences. Under severe irradiation, the correlation length of the anion sublattice saturates to a very small value of a few nanometers. What are the consequences of this small correlation length characterizing the anion sublattice on the energy dissipation in the material during the irradiation? The fluctuation-dissipation theorem [48,49] establishes a relation between equilibrium correlation functions and linear response functions. Perhaps we can establish a moot analogy between this behavior and what happens in a turbulent flow [50]. Physically, energy is dissipated because of the work done by the fluctuating viscous stresses in resisting deformation of the fluid material

by the fluctuating strain rates. When turbulence is present, it usually dominates all other flow phenomena, and it results in increased energy dissipation, mixing, heat transfer, and drag. The dissipation of turbulence energy mostly takes place at the smallest turbulence scales, and those scales can be characterized by the so-called Kolmogorov microscale defined by $\eta_K = (\frac{\nu^3}{\varepsilon})^{1/4}$, where ε is the average rate of dissipation of turbulence kinetic energy per unit mass, and ν is the kinematic viscosity of the fluid. In atmospheric motions, typical values of the Kolmogorov microscale range from 0.1 to 10 mm. In laboratory flows, where the overall scale of the flow is greatly reduced, much smaller values of η_K are not uncommon. Viscous scales [operating on a time scale of $t_K = (\frac{\nu}{\varepsilon})^{1/2}$] dissipate rapidly any energy sent down to them by the nonlinear processes of scale-to-scale energy transfer. The coarse-grained approach for the spatial averaging of the cation sublattice seems then an effective way for introducing field fluctuations and dissipation described by the correlation length of the anion sublattice. The very short correlation length describing the spatial distributions of the topological defects in this system, where otherwise the crystallinity continues to be described by a significantly longer characteristic correlation length, can explain why the nonequilibrium dynamics of this open system is so effective in dissipating the energy of the irradiation process, allowing the system to remain crystalline at fluences where many other fluorite-related counterpart systems amorphize. To some extent, $Gd_2Ce_2O_7$ behaves like a functional material because its topological defects effectively lead to very strong enhancements of the radiation resistance properties. Microdomain walls create localized sinks that can efficiently absorb part of the defect concentrations generated by irradiation but also effectively dissipate the energy in the Kolmogorov picture [50], retaining much of the long-range periodic properties of the cation sublattice of the pristine structure.

This highly effective radiation response of this material might be universal to the class of oxygen-deficient fluorites displaying a distinctive O vacancy ordering in the anion sublattice without any particular cation ordering, providing the decoupling of the order characteristics of the two sublattices and opening the way for a coarse-grained approach to this system. The existence of mobile antiphase boundaries within a coarse-grained periodic system seems to provide an extremely effective pathway to dissipate the energy introduced by the irradiation process, thus avoiding the amorphization of the crystal structure that is typically observed in fluorite-related systems where the cations are ordered.

[1] O. T. Sørensen, *Nonstoichiometric Oxides*, 1st Edition (Academic Press, New York, 1981).

[2] D. J. M. Bevan, W. W. Barker, R. L. Martin, and T. C. Parks, Mixed oxides of the type MO_2 (fluorite)-M_2O_3. Part 2: Non-stoichiometry in ternary rare-earth oxide systems, in *Proceedings of the Fourth Conference on Rare Earth Research* (Gordon and Breach, New York, 1965), pp. 441–468.

[3] J. O. Sawyer, B. G. Hyde, and L. Eyring, Fluorite-related homologous series in the rare earth oxides, Bull. Soc. Chim. France **4**, 1190 (1965).

[4] B. G. Hyde, D. J. M. Bevan, and L. Eyring, On the praseodymium + oxygen system, Philos. Trans. R. Soc. A **259**, 583 (1966).

[5] G. Brauer, Structural and solid state chemistry of pure rare earth oxides and hydroxides, in *Progress in the Science and Technology of the Rare Earths* (Pergamon, Oxford, 1966), Vol. 3, pp. 434–458.

[6] D. J. M. Bevan and E. Summerville, Mixed rare earth oxides, in *Handbook on the Physics and Chemistry of Rare Earths*, edited by K. A. Gschneidner, Jr., and L. Eyring (North-Holland, Amsterdam, 1979), Vol. 3, Chap. 28, pp. 401–524.

[7] J. D. McCullough and J. D. Britton, X-ray studies of rare earth oxide systems II, J. Am. Chem. Soc. **74**, 5225 (1952).

[8] I. F. Ferguson and P. G. T. Fogg, The oxides of uranium. Part VIII. The system uranium dioxide-yttria, J. Chem. Soc. 3679 (1957).

[9] G. Brauer and H. Gradinger, Über heterotype Mischphasen bei Seltenerdoxyden. I, Z. Anorg. Allg. Chem. **276**, 209 (1954).

[10] G. Brauer and H. Gradinger, Über heterotype Mischphasen bei Seltenerdoxyden. II. Die Oxydsysteme des Cers und des Praseodyms, Z. Anorg. Allg. Chem. **277**, 89 (1954).

[11] G. Brauer and U. Holtschmidt, Über die Oxyde des Cers. III, Z. Anorg. Allg. Chem. **279**, 129 (1955).

[12] P. Kunzmann and L. J. Eyring, On the crystal structures of the fluorite-related intermediate rare-earth oxides, J. Solid State Chem. **14**, 229 (1975).

[13] Z. C. Kang, Lanthanide higher oxides: the contribution of Leroy Eyring, in *Handbook on the Physics and Chemistry of Rare Earths*, edited by K. A. Gschneidner, Jr., J.-C. G. Bünzli, and V. K. Pecharsky (Elsevier, Amsterdam, 2008), Vol. 38, Chap. 236.

[14] Y. Ikuma, S. Anandan, and K. Niwa, Lattice parameter, defect concentration and oxygen diffusion in ceria solid solutions, Trans. Mat. Res. Soc. Japan **35**, 485 (2010).

[15] D. L. Drey, E. C. O'Quinn, T. Subramani, K. Lilova, G. Baldinozzi, I. M. Gussev, A. F. Fuentes, J. C. Neuefeind, M. Everett, D. Sprouster, A. Navrotsky, R. C. Ewing, and M. Lang, Disorder in $Ho_2Ti_{2-x}Zr_xO_7$: pyrochlore to defect fluorite solid solution series, RSC Adv. **10**, 34632 (2020).

[16] K. Wurst, E. Schweda, D. J. M. Bevan, J. Mohyla, K. S. Wallwork, and M. Hofmann, Single-crystal structure determination of $Zr_{50}Sc_{12}O_{118}$, Solid State Sci. **5**, 1491 (2003).

[17] S. Meyer, E. Schweda, M. N. J. Martinez, H. Boysen, M. Hoelzel, and T. Bredow, Neutron powder diffraction study and DFT calculations on the structure of $Zr_{10}Sc_4O_{26}$, Z. Kristallogr. **224**, 539 (2009).

[18] M. R. Thornber, D. J. M. Bevan, and J. Graham, Mixed oxides of the type MO_2(fluorite)-M_2O_3, III. Crystal structures of the intermediate phases $Zr_5Sc_2O_{13}$ and $Zr_3Sc_4O_{12}$, Acta Crystallogr. B **24**, 1183 (1968).

[19] M. Lang, F. Zhang, J. Zhang, J. Wang, J. Lian, W. Weber, B. Schuster, C. Trautmann, R. Neumann, and R. Ewing, Review of $A_2B_2O_7$ pyrochlore response to irradiation and pressure, Nucl. Instrum. Methods Phys. Res., Sect. B **268**, 2951 (2010).

[20] Y. H. Li, B. P. Uberuaga, C. Jiang, S. Choudhury, J. A. Valdez, M. K. Patel, J. Won, Y.-Q. Wang, M. Tang, D. J. Safarik, D. D. Byler, K. J. McClellan, I. O. Usov, T. Hartmann, G. Baldinozzi, and K. E. Sickafus, Role of Antisite Disorder on Preamorphization Swelling in Titanate Pyrochlores, Phys. Rev. Lett. **108**, 195504 (2012).

[21] J. Shamblin, M. Feygenson, J. Neuefeind, C. L. Tracy, F. Zhang, S. Finkeldei, D. Bosbach, H. Zhou, R. C. Ewing, and M. Lang, Probing disorder in isometric pyrochlore and related complex oxides, Nat. Mater. **15**, 507 (2016).

[22] D. Simeone, G. J. Thorogood, D. Huo, L. Luneville, G. Baldinozzi, V. Petricek, F. Porcher, J. Ribis, L. Mazerolles, L. Largeau, J. F. Berar, and S. Surble, Intricate disorder in defect fluorite/pyrochlore: a concord of chemistry and crystallography, Sci. Rep. **7**, 3727 (2017).

[23] G. Pilania, B. Puchala, and B. Uberuaga, Distortion-stabilized ordered structures in $A_2BB'O_7$ mixed pyrochlores, npj Comput. Mater. **5**, 7 (2019).

[24] V. Grover, S. N. Achari, and A. K. Tyagi, Structural analysis of excess-anion C-type rare earth oxide: A case study with $Gd_{1-x}Ce_xO_{1.5+x/2}$ ($x = 0.20$ and 0.40), J. Appl. Crystallogr. **36**, 1082 (2003).

[25] M. K. Patel, G. Baldinozzi, J. A. Aguiar, J. A. Valdez, S. C. Vogel, and K. E. Sickafus, Structural analysis of $Gd_2Ce_2O_7$, MRS Proc. **1743**, Mrsf14-1743-ww05-03 (2015).

[26] W. Feller, *An Introduction to Probability Theory and its Applications*, 3rd Edition (John Wiley and Sons, New York and London, 1968), Vol. 1.

[27] J. F. Ziegler and J. P. Biersack, The stopping and range of ions in matter, in *Treatise on Heavy-Ion Science*, edited by D. A. Bromley (Springer, Boston, 1985).

[28] J. F. Berar and G. Baldinozzi, XND code: from x-ray laboratory data to incommensurately modulated phases. Rietveld modeling of complex materials, IUCr CPD Newsletter **20**, 3 (1998).

[29] See Supplemental Material at http://link.aps.org/supplemental/10.1103/PhysRevMaterials.6.013610 for details of x-ray and TEM diffraction.

[30] G. Baldinozzi, J.-F. Berar, and G. Calvarin, Rietveld refinement of two-phase Zr-doped Y_2O_3, Mater. Sci. Forum **278–281**, 680 (1998).

[31] G. Baldinozzi, J. F. Berar, M. Gautier Soyer, and G. Calvarin, Segregation and site selectivity in Zr-doped Y_2O_3, J. Phys.: Condens. Matter **9**, 9731 (1997).

[32] SingleCrystalTM: a single-crystal diffraction program for Mac and Windows. CrystalMaker Software Ltd, Oxford, England (www.crystalmaker.com).

[33] R. B. Neder, F. Frey, and H. Schulz, Diffraction theory for diffuse scattering by correlated microdomains in materials with several atoms per unit cell, Acta Crystallogr. A **46**, 792 (1990).

[34] R. J. D. Tilley, Correlation between dielectric constant and defect structure of non-stoichiometric solids, Nature (London) **269**, 229 (1977).

[35] A. M. Stoneham and P. J. Durham, The ordering of crystallographic shear planes: theory of regular arrays, J. Phys. Chem. Solids **34**, 2127 (1973).

[36] J. G. Allpress and H. J. Rossell, A nanodomain description of defective fluorite-type phases $Ca_xM_{1-x}O_{2-x}$, ($M =$ Zr, Hf; $x = 0.1$–0.2), J. Solid State Chem. **15**, 68 (1975).

[37] M. P. Van Dijk, F. C. Mijlhoff, and A. J. Burggraaf, Pyrochlore nanodomain formation in fluorite oxides, J. Solid State Chem. **62**, 377 (1986).

[38] M. Fevre, A. Finel, and R. Caudron, Local order and thermal conductivity in yttria-stabilized zirconia, I. Microstructural investigations using neutron diffuse scattering and atomic-scale simulations, Phys. Rev. B **72**, 104117 (2005).

[39] L. Van Hove, Correlations in space and time and Born approximation scattering in systems of interacting particles, Phys. Rev. **95**, 249 (1954).

[40] M. Kardar, *Statistical Physics of Fields* (Cambridge University Press, Cambridge, 2007).

[41] E. C. O'Quinn, K. E. Sickafus, R. C. Ewing, G. Baldinozzi, J. C. Neuefeind, M. G. Tucker, A. F. Fuentes, D. Drey, and M. K. Lang, Predicting short-range order and correlated phenomena in disordered crystalline materials, Sci. Adv. **6**, eabc2758 (2020).

[42] H. Jagodzinski and F. Frey, Disorder diffuse scattering of x-rays and neutrons, in *International Tables for Crystallography*, edited by U. Shmueli (2006), Vol. B, Chap. 4.2, pp. 407–442.

[43] J. Brunet and K. E. Gubbins, General theory of the long range pair correlation function, J. Chem. Phys. **49**, 5265 (1968).

[44] M. K. Patel, K. E. Sickafus, and G. Baldinozzi, Divergent short- and long-range behavior in ion-irradiated δ-$Sc_4Hf_3O_{12}$, Phys. Rev. Materials **4**, 093605 (2020).

[45] W. H. Hall, X-ray line broadening in metals, Proc. Phys. Soc. A **62**, 741 (1949).

[46] T. Ungar, Micro structural parameters from x-ray diffraction peak broadening, Scr. Mater. **51**, 777 (2004).

[47] W. Kauzmann, The nature of the glassy state and the behavior of liquids at low temperatures, Chem. Rev. **43**, 219 (1948).

[48] J. Weber, Fluctuation dissipation theorem, Phys. Rev. **101**, 1620 (1956).

[49] J. P. Hansen, F. Joly, and I. R. McDonald, Self-diffusion, interdiffusion and long wavelength plasma oscillations in binary ionic mixtures, Physica A **132**, 472 (1985).

[50] P. Manneville, Dissipative structures and weak turbulence, in *Chaos—The Interplay Between Stochastic and Deterministic Behaviour*, edited by P. Garbaczewski, M. Wolf, and A. Weron. Lecture Notes in Physics (Springer, Berlin, 1995), Vol. 457.